Theoretical and Experimental Study of Particle Distribution from Magnetron Sputtering with Masks for Accurate Thickness Profile Control

Yingna Shi [1,2], **Qiushi Huang** [1,2,*], **Runze Qi** [1,2], **Zhengxiang Shen** [1,2], **Zhong Zhang** [1,2] and **Zhanshan Wang** [1,2]

1 MOE Key Laboratory of Advanced Micro-Structured Materials, No.1239 Siping Road, Shanghai 200092, China; shiyingna192514@126.com (Y.S.); qrz@tongji.edu.cn (R.Q.); shenzx@tongji.edu.cn (Z.S.); zhangzhongcc@tongji.edu.cn (Z.Z.); wangzs@tongji.edu.cn (Z.W.)
2 Institute of Precision Optical Engineering, School of Physics Science and Engineering, Tongji University, Shanghai 200092, China
* Correspondence: huangqs@tongji.edu.cn

Abstract: Differential deposition and profile coating are two common deterministic fabrication methods for figure correction of high-precision mirrors. The generation of the desired particle distribution on the substrate as the growing function is an important prerequisite, especially for two-dimensional correction. A model of particle distribution considering the etched ring shape, mask structure, and mask distance between the target and substrate is established. The model is verified by deposition experiments using a series of circular holes with different hole sizes and distances of the mask from the substrate. According to the model, a smallest deposition beam width of 2.79 mm can be obtained using a hole with a 3 mm diameter. The shape of the particle distribution gradually changes from convex to concave as the mask moves away from the substrate for different holes. A two-dimensional figure correction of a flat mirror was demonstrated using a hole with a 6 mm diameter. The peak-to-valley (PV) value is reduced from 74.23 nm to 10.09 nm, and the root mean square (RMS) value is reduced from 18.38 nm to 1.36 nm within a 130 mm × 20 mm area. The model could provide useful guidance for high-precision two-dimensional figure correction applications.

Keywords: magnetron sputtering; particle distribution; figure correction; model simulation; two-dimensional; different spatial frequency

---

1. Introduction

Given the fast development of synchrotron radiation and free-electron laser facilities, the demand for high-precision X-ray optical components has greatly increased, and the requirements for optical components are very high. Figure correction is generally achieved by deterministic removal or addition methods to reduce the deviation between the fabricated figure and the designed one. The removal methods mainly include plasma chemical vaporization machining (PCVM) combined with elastic emission machining (EEM) [1–3], and ion beam figuring (IBF) [4–6]. PCVM combined with EEM can create mirror surfaces with a figure error (peak-to-valley (PV)) as low as 1 nm and a lateral resolution close to 0.1 mm [7]. IBF provides both high accuracy and high efficiency, and a figure error of 0.5 μrad (root mean square (RMS)) has been widely realized [8]. The addition methods include differential deposition [9–13] and profile coating [14–19] based on modern physical deposition techniques. These are also high-precision and high-efficiency correction techniques, and expensive substrates can be reused to create different profiles since the added correction layer can be removed with different methods [20–22]. Differential deposition and profile coating are usually performed by magnetron sputtering instead

of electrodeposition [23], cathodic arc evaporation [24], and electromagnetic venetian blind plasma filter [25] due to the ultra-smooth surface requirement of precision figure correction. The differential deposition has generated an accurate thickness profile with a deviation of less than 0.3 nm (RMS) from the designed one on a flat substrate [9]. Profile coating has been used to fabricate focusing mirrors for synchrotron radiation facilities and space telescopes, using Au, Pt, or Ni. The smallest RMS deviation between the deposited profile and the designed ellipse was below 0.41 nm [15]. Coating methods are easily implemented using standard coating machines, so there are gradually more people working on these methods [9–18].

Several different processes have been studied to perform differential deposition and profile coating. There are two ways to use the differential deposition technique. One is that the target power is adjusted according to the designed thickness correction profile (i.e., higher power for a larger thickness) when the substrate passes by the magnetron cathode at a constant speed [13], as shown in Figure 1a. The other way is to vary the motion speed of the substrate while the target power is fixed [9]. In above two ways, a mask with a slit is placed between the target and the substrate, where the width of the slit changes the particle distribution contour on the substrate and the size and shape of the contour influences the smallest feature that can be corrected during the figuring process, as shown in Figure 1b. The one-dimensional corrected thickness profile is obtained along the direction of the substrate motion [10–12]. As for profile coating, the target power and the speed of the substrate are kept constant [14]. A mask is placed between the target and substrate, and the opening width of the mask at different positions perpendicular to the substrate motion direction determines the coating thickness at the corresponding positions [19], as shown in Figure 1c. A one-dimensional correction profile is obtained perpendicular to the direction of substrate movement because of different opening widths at different positions on the mask, and the coating thickness along the substrate motion direction is uniform due to the constant-speed motion of the substrate [15–18]. In both differential deposition and profile coating, a dedicated mask is used to modify the spatial distribution of the deposited particles and generate a growing function for figuring.
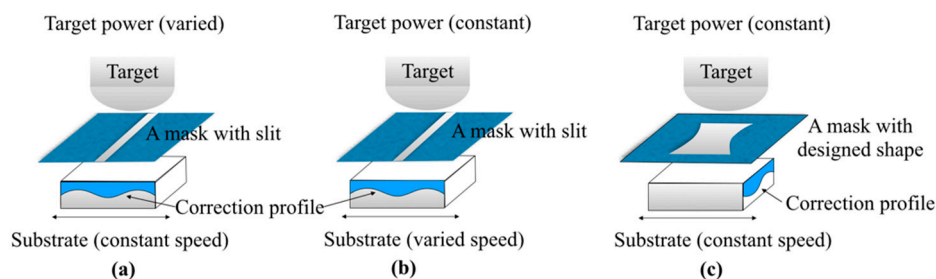
Figure 1. Different processes of coating methods. (**a**) Differential deposition (varied target power). (**b**) Differential deposition (varied substrate speed). (**c**) Profile coating.

The previous studies performed on coating-based figuring are limited to one-dimensional corrections. The X-ray deflection or focusing mirrors used in beamlines mostly require an accurate two-dimensional figure which demands two-dimensional shape corrections. In this case, having a good understanding and accurate control of the sputtered particle distribution on the substrate is important to achieve the desired 2D profile. Particle distribution on the substrate is related to the shape of the etched ring, angular distribution of the sputtered atoms, and the particle transport process. Particles are mainly sputtered out of the etched ring on the target, and the etched profile can be approximated by a Gaussian distribution [26,27]. Yamazaki et al. found that the uniformity of film thickness varied by changing the distribution of the erosion depth of the target [28]. Ekpt et al. discovered that the deposited contour on the substrate is greatly affected by the shape of the etched ring on the target. When the substrate was 15 mm away from the target surface, the deposited contour on the substrate appeared to be a concave shape, and the smaller the width of the etched ring, the more obvious the concave shape was [29]. According to the random collision cascade theory, the angular distribution of

sputtered particles is usually assumed to follow a cosine distribution [26,29,30]. However, the predicted deposited profile by the cosine distribution deviates from experimentally deposited profiles in some cases, and a revised angular distribution has been developed under different conditions [28,30–32]. Anderson et al. developed the cosine distribution as the $\cos^n\theta$ distribution when studying the angular distribution of particles sputtered from Cu, Pt, and Ge targets by keV Ar$^+$ ion bombardment, and the simulation results fitted the experimental results very well [32]. Yamazaki et al. also used a $k\cos^n\theta$ distribution to explain the nonuniformity of the thickness and composition of the MoSi$_x$ sputtering films. The values of k and n of Mo and Si are calculated, respectively, to coincide with the thickness and composition distribution of the experimental results [28]. The angular distribution can also be affected by temperature. Zhang et al. studied the angular distribution of sputtered indium particles at different sample temperatures of 25 °C and 70 °C, which was found to follow the function of $a\cos\theta + b\cos^n\theta$ [30]. Particle transport is usually a complex process due to gas scattering [33,34]. In some cases, the effect of gas scattering can be neglected; then the process is simplified to collisionless transport, that is, particle transport from the target to the substrate in a straight line [26,29].

Although theoretical and experimental studies have been performed on the distribution of sputtered particles from the target, there is no systematic research about the effect of a mask on the sputtered particle distribution and the formation of a certain growth function. Based on the previous theoretical model of particle sputtering, the change of sputtered particle distribution under simple circular masks was studied both theoretically and experimentally. According to the experimentally verified model, the particle distribution contour on the substrate can be better controlled, and theoretical simulation of a two-dimensional shape correction was demonstrated.

In this paper, the model of particle sputtering when adding a mask between the target and substrate is detailed in Section 2. The experiments using masks with different hole sizes and different positions to verify the established model are shown in Section 3. The experiment results and the applications of the established model are discussed in Section 4.

2. Modeling

In order to establish the model to obtain the particle distribution on the substrate, three parts must be considered, namely, the positional probability of particles sputtered out of target which relates to the etched ring profile, the angular distribution of the sputtered particles, and the sputtered particles that pass through the mask and deposited on the substrate.
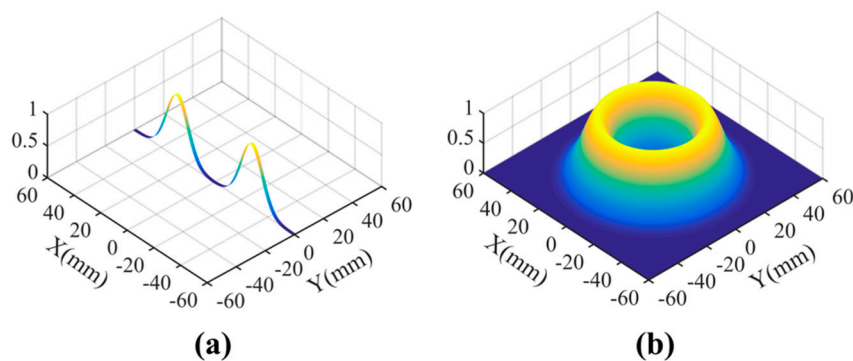
2.1. Positional Probability of Particles Sputtered out of the Circular Target

A 4-inch circular target was used in our model. Figure 2a shows a photo of the circular target with an etched ring where the cross-section is near Gaussian shape, as shown in Figure 2b. The particles were assumed to sputter from the target surface based on the shape of the etched ring. A deeper etched depth means that more particles were sputtered out from this position due to the confinement of the magnetic field. According to the cross-section of the etched ring, the positional probability of particles sputtered out of the target along the radial direction is expressed by Equation (1) [27], where μ is the expected value of Gaussian distribution, determined by the radius of the etched ring in the model, and σ is the standard deviation of Gaussian distribution and determines the amplitude of the distribution. In the model, σ is jointly affected by the depth and width of the etched ring. As shown in Figure 3a, the two-dimensional positional probability distribution of sputtered particles along the radial direction is calculated from the etched ring, and Figure 3b shows the three-dimensional positional probability distribution obtained by rotation.

$$P(x) = \frac{1}{\sqrt{2\pi}\sigma} e^{\frac{-(x-\mu)^2}{2\sigma^2}} \tag{1}$$
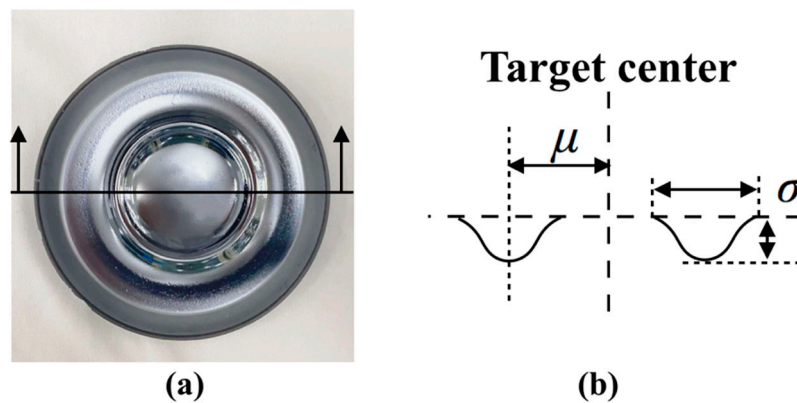
Figure 2. (**a**) Photo of the circular target. (**b**) Cross-section of the target, where μ is determined by the radius of the etched ring, and σ is related to the depth and width of the etched ring.

Figure 3. (**a**) Two-dimensional positional probability distribution of sputtered particles along the radial direction, calculated from the etched ring. (**b**) Three-dimensional positional probability distribution obtained by rotation.

2.2. Angular Distribution of the Sputtered Particles

Angular distribution describes the probabilities of the particles sputtered out at different angles. In our model, angular distribution is based on random collision cascade theory, which shows that the envelope of the angular distribution is an ellipse. This is the most commonly used conventional model in the study of angular distribution [26,28,32]. As shown in Figure 4, the length of the arrow in the ellipses indicates the probability of particles sputtered out from this direction. There are generally three situations with different α values, which depend on the cathode power and target material [26]. According to the angular distribution, every sputtered particle has an angular probability weight due to a different emitting angle, which can be defined by the following formula:

$$F(\theta_T) = \frac{\cos(\theta_T)}{\alpha^2 + (1-\alpha^2)\cos^2(\theta_T)} \tag{2}$$

where θ_T is the angle between the particle exit direction and the target surface normal vector and α is the ratio of the major to minor axis of the ellipse, which allows one to fit the theoretical distribution to the experimental data. Comparing the experiments, α is 1.6 in our model.
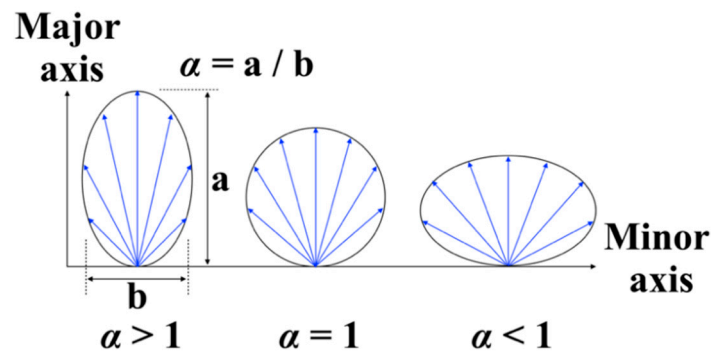
Figure 4. Three different situations of angular distribution.

2.3. Straight Line Transport of Sputtered Particles Passing through the Mask

After the particles are sputtered out of the target, they pass through the mask, and finally are deposited on the substrate. The mean free path of the transport process under our experimental conditions was calculated, which was 85 mm. Comparing the target–substrate distance of 70 mm in our experiment, the transport process was assumed to be straight-line transport, and particle scattering was not considered. As shown in Figure 5, the target surface is on plane 1, the mask is on plane 2, and the substrate is on plane 3. The distance between plane 1 and plane 2 is d_1, and the distance between plane 2 and plane 3 is d_2. A particle from the point P_i on the target surface passes through the point P_j within the mask hole and finally is deposited at point P_k on the substrate. X_i, Y_i, X_j, and Y_j are the coordinate values of P_i and P_j. X_k and Y_k are the coordinate values of P_k. When the positions of P_i and P_j and the position of the mask between the target and the substrate are definite, the position of P_k according to the geometric linear relationship can be obtained, as shown in Equation (3).

$$
\begin{aligned}
X_k &= \frac{(X_j - X_i)d_2}{d_1} + X_j \\
Y_k &= \frac{(Y_j - Y_i)d_2}{d_1} + Y_j
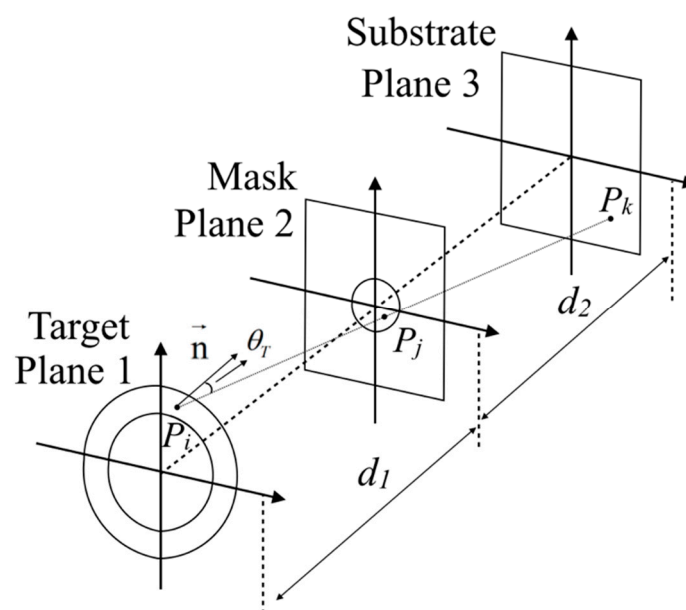\end{aligned}
\tag{3}
$$

Figure 5. Schematic diagram of the straight-line transport of sputtered particles passing through the mask.

The sputtered particles are emitted out of the target surface according to the positional probability, and N is the total number of sputtered positions on the target. M is the number of positions randomly generated within the opening range on the mask. For each of the sputtered positions on the target, M new random positions are generated within the opening range on the mask. In this way, eventually, N × M positions of the sputtered particles are obtained on the substrate.

Due to the angular distributions, the weighting of each sputtered particle is different. The emission angles of sputtered particles can be calculated by their coordinates on the target, and the substrate, and then the angular weighting can be obtained by Equation (2). The two-dimensional deposited thickness distribution on the substrate is obtained by integrating the contribution of all the sputtered particles passing through the mask.

3. Experiments

The experiments using the mask with a series of circular holes was conducted to verify the established model. Si coatings were deposited on Si substrates by direct current magnetron sputtering [35]. The background pressure before the deposition was lower than 3×10^{-4} Pa. High-purity Ar (99.999%) was used as the working gas. The Ar flow rate is 5 SCCM (standard cubic centimeter per minute), the working pressure was fixed at 0.2 Pa during deposition, and the target power is 40 W. A mask was placed between the target and the substrate. Figure 6 shows a photo of the mask. There are five circular holes of the same size on the mask, and the distance between the centers of the adjacent holes was 20 mm here. The center hole locates approximately above the center of the sputtering target. Five holes on the mask were used to obtain the deposited thickness distribution at the center and the edge of the substrate. The mask was made by machining, and the thickness of the mask was 1 mm.
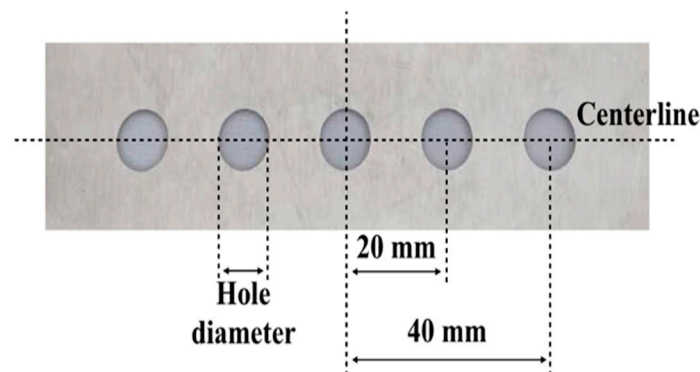

Figure 6. Schematic diagram of the hole distributions on the mask.

The substrate was half shielded along the centerline before the deposition, so there are only half circles on the experimental sample, and a linear step was formed along the centerline, as shown in Figure 7a. The step height represents the deposited thickness at the corresponding position, and the step height was measured by an optical profilometer (Contour GT-X3, Bruker, Billerica, MA, USA) along the centerline to obtain a one-dimensional profile [36]. A 10× objective lens was used in the measurements, and the size of the test area was 0.62 × 0.47 mm here [37]. Figure 7b is a result of the step measurement, and the step height can be obtained by dealing with the measurement result, as shown in Figure 7c.

There were two variables when the experiments were conducted to verify the established particle distribution model, one was the hole size on the mask, and the other was the distance of the mask between the target and the substrate. The detailed experimental parameters are listed in Table 1.
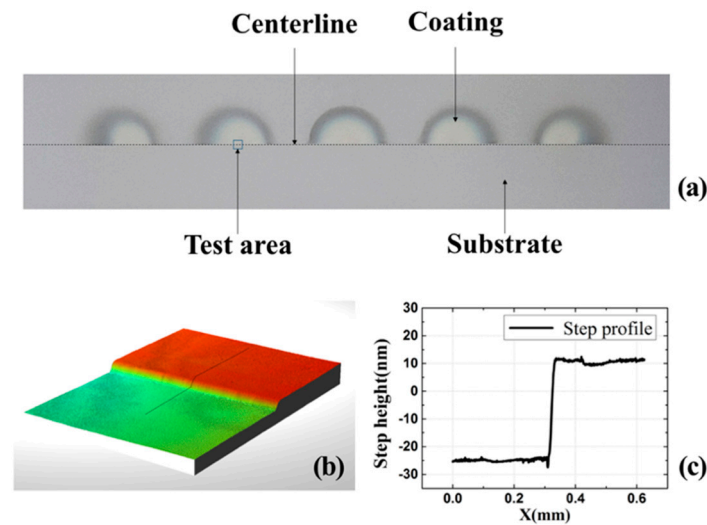
Figure 7. Step measurement by the optical profilometer. (**a**) Photo of the experimental sample with a step. (**b**) Measurement result of the optical profilometer. (**c**) Step height found by the results of the optical profilometer.

Table 1. Detailed experimental parameters. The hole size on the mask and the distance of the mask between the target and the substrate are two variables.

Variables	Target–Substrate Distance (mm)	d_1 (mm)	d_2 (mm)	Hole Diameter (mm)	Deposition Time (s)
Hole size	70	62	8	3	5400
	70	62	8	6	2100
	70	62	8	10	900
Mask distance	70	62	8	6	2100
	70	57	13	6	2100

4. Experimental Results and Discussion

4.1. Comparison of Different Hole Sizes on the Masks

In Figure 8, the experimental and simulated results of masks with different hole sizes were compared. The top images are photographs of the experimental samples, the middle are particle distributions on the substrate simulated by the model, and the bottom show the cross-section along the centerline of the deposited area, where the solid lines are from the simulations, and the dots are from the step measurements. The error of the step measurements, which is ±5 nm, is given based on the repeated measurements, and the model parameters are adjusted according to the mean value of the step measurements to obtain the simulation curves. Figure 8a–c corresponds to hole diameters of 3, 6, and 10 mm. The experimental and simulated results are in good agreement in terms of location, size, and contour shape. The particle distribution is symmetrical at the center, and the symmetry deteriorates as the location shifts toward the edge. The asymmetry of particle distribution, which is caused by the angular distribution of the sputtered particles, is unfavorable in the process of shape correction, and the program simulation can guide us to take the appropriate position of the target surface for shape correction.
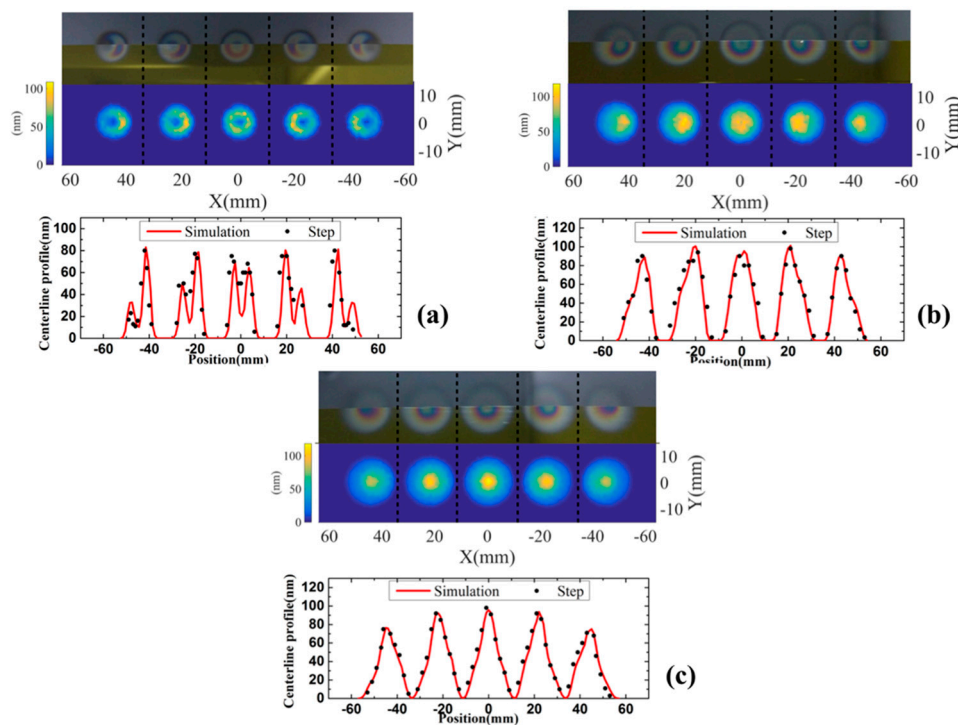
Figure 8. Comparison of different hole sizes on the masks. (**a**) Hole diameter of 3 mm, d_1 = 62 mm, d_2 = 8 mm. (**b**) Hole diameter of 6 mm, d_1 = 62 mm, d_2 = 8 mm. (**c**) Hole diameter of 10 mm, d_1 = 62 mm, d_2 = 8 mm.

When the hole diameter was 3 mm, the particle distribution contour was concave, while the contour was convex when the hole diameters were 6 mm and 10 mm. The concave shape is caused by the ring shape of the etched area and the limitation of hole size, similar to the small hole imaging principle. The concave shape is similar to the ring shape of the etched area on the target. The etched ring on the target can be regarded as the object, and the particle distribution contour on the substrate can be regarded as the image. When the distance from the hole to the substrate is the same, a smaller hole will "image" the shape of the sputtering source to the substrate with better resolution, so an obvious concave contour can be seen on the substrate when the diameter of the hole is 3 mm. The cross-sectional profiles along the centerline from both the step measurement and simulation were in good agreement when the particle distribution contours were convex. When the contour was concave, the cross-sectional profile from the simulation deviated a little from that of the step measurement at the edges. This can be explained by two reasons. First, it is considered that the step is difficult to measure exactly when the coating thickness is too thin and changes sharply. Second, when the hole size is very small, the mask thickness will affect particle transport, and the actual situation will deviate from the straight-line transport assumed in the model. When the hole on the mask deviates from the center of the target surface, the edge scattering effect caused by this mask thickness will be more obvious, so the deviation at the edge will be larger. Even with some deviations, the trend of measured contours is mostly consistent with theory. The correction rate is also of great concern to us. When the diameters of the hole were 3, 6, and 10 mm, the maximum deposition rates of the center hole were 0.015, 0.047, and 0.109 nm/s, respectively. Obviously, a smaller beam shape comes with a lower correction efficiency.

4.2. Comparison of Different Distances of the Mask between the Target and the Substrate

In Figure 9, the experimental and simulated results of the mask with different positions between the target and substrate when the hole diameter remained at 6 mm were compared. The top images are photographs of the experimental samples, the middle is the particle distributions on the substrate simulated by the model, and the bottom is the cross-sectional profiles along the centerline, where the

solid lines are from the simulations, and the dots are from the step measurements. The error of the step measurements, which is ±5 nm, is given based on the repeated measurements, and the model parameters are adjusted according to the mean value of the step measurements to obtain the simulation curves. For Figure 9a, $d_1 = 62$ mm, $d_2 = 8$ mm, while for Figure 9b, d_1 is reduced by 5 mm and d_2 is increased by 5 mm. After increasing the distance of the mask from the substrate, the particle distribution contour on the substrate changed from convex to concave, and the contour size became larger. The beam width of the center distribution contour, which present the width of half maximum thickness of the beam profile, also increased from 10.54 mm to 17.39 mm. This phenomenon can also be explained by the principle similar to small hole imaging. For holes of the same size, when the hole is close to the substrate, the imaging of the shape characteristic of the sputtering source cannot be clearly resolved on the substrate. When the hole is far away from the substrate, the shape characteristics of the sputtering source can appear on the substrate clearly, so an obvious concave contour can be seen on the substrate when the hole that is 6 mm in diameter is far away from the substrate.
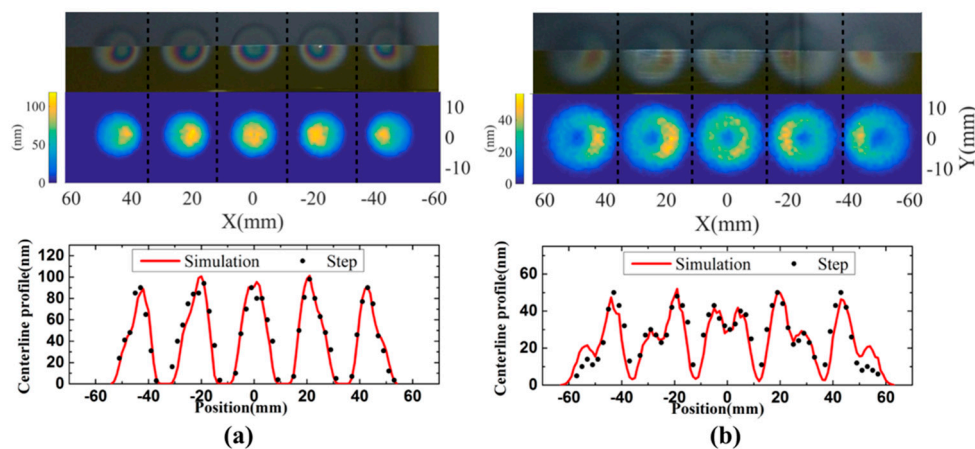

Figure 9. Comparison of different distances of the mask between the target and the substrate. (**a**) Hole diameter of 6 mm, $d_1 = 62$ mm, $d_2 = 8$ mm. (**b**) hole diameter of 6 mm, $d_1 = 57$ mm, $d_2 = 13$ mm.

4.3. Applications of the Established Model

According to the established model, the particle sputtering from the target surface, the angular distribution of the sputtered particles, and the mask all affect the particle distribution on the substrate. In the model, the target sputtering is determined by the parameters of the etched ring on the target, while the angular distribution of the sputtered particles is determined by the experimental conditions, such as the target material and sputtering power. When the target and experimental parameters are determined, it is simplest and most effective to realize the regulation of the particle distribution on the substrate by adjusting the parameters of the mask. Therefore, in this part, the influence of the hole size and the distance of the mask from the substrate on the particle distribution on the substrate was studied in more detail. Based on the understanding of the impact of the different parameters on the contour on the substrate, suitable hole size and mask distance was chosen for the subsequent figure correction of different spatial frequencies.

The particle distribution contour on the substrate with different distances between the mask and substrate ranging from 2 mm to 12 mm when the hole diameters were 3 mm and 6 mm were simulated. A mask with a single hole corresponding to a target center was used to obtain the symmetrical contour. The deposition time for all conditions is the same, which is 2100 s. Figure 9 shows the simulation results of the particle distribution contour on the substrate with different distance between mask and substrate. Figure 10a,b are the results when the hole diameters were 3 mm and 6 mm, respectively. The left column shows the two-dimensional contour, and the right row shows the cross-sectional profile along the centerline. As the distance from the mask to the substrate changed from 2 mm to 12 mm, the beam width of the cross-section profile changed from 2.79 mm to 14.84 mm for the 3 mm

in diameter hole, and from 5.43 mm to 16.26 mm for the 6 mm in diameter hole. At the same time, when the mask was close to the substrate, the contour was convex, and as the mask was far away from the substrate, the contour gradually became concave. The transition from convex to concave happened when the distance from the mask to the substrate was around 6 mm for a 3 mm in diameter hole, and the transition happened when the distance from the mask to the substrate was approximately 10 mm for a 6 mm in diameter hole.
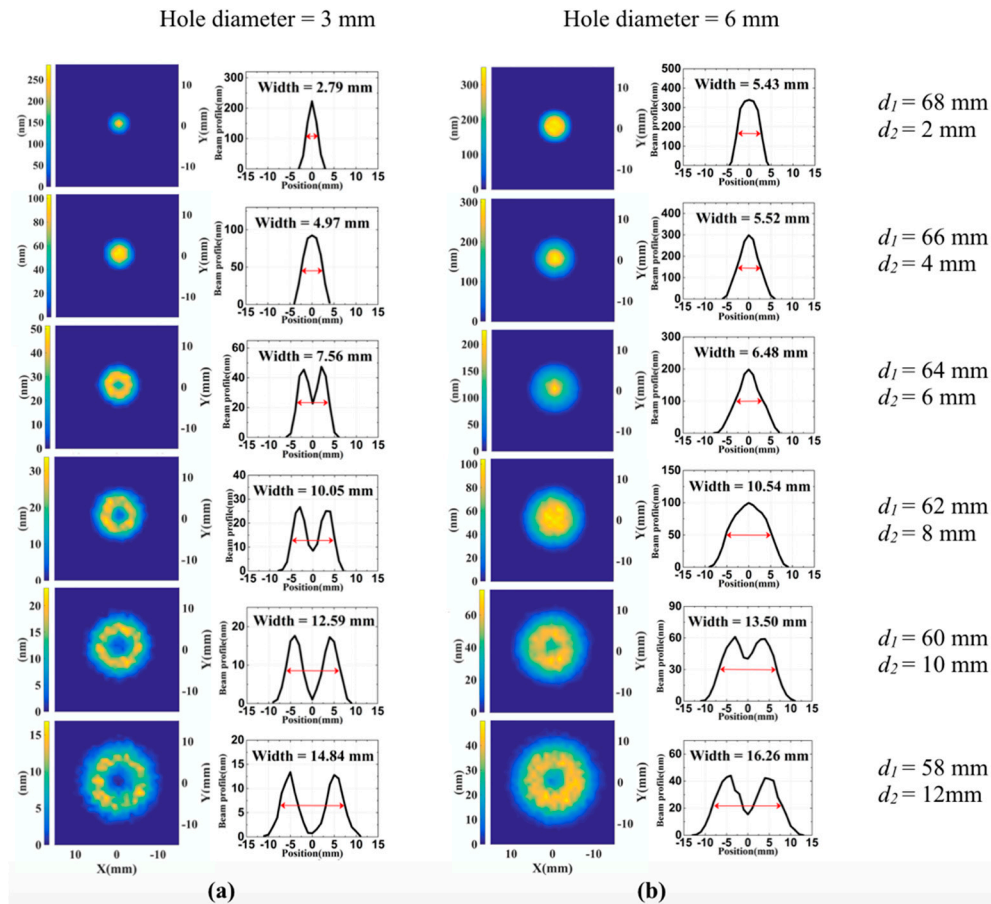

Figure 10. Simulation results of the particle distribution contour on the substrate with different distances between the mask and substrate. (**a**) Hole diameter of 3 mm. (**b**) Hole diameter of 6 mm.

Based on the simulation results, a two-dimensional correction of a flat mirror was simulated. The initial shape of the mirror was obtained by an interferometer, whose size was 130 × 20 mm, as shown in Figure 11a. The correction by using a single hole with a 6 mm diameter was simulated. The hole position corresponds to the center one of the masks studied in Section 4, and the distances from the mask to the target and substrate were 62 mm and 8 mm, respectively. The beam width of the distribution contour on the substrate was 10.54 mm. The cross-sectional profile was convex, and the distribution was similar to Gaussian distribution (Figure 10b), which is suitable for two-dimensional figure correction by stitching. Figure 12 shows the schematic diagram of the correction process. The 20-mm-wide two-dimensional surface was divided into three lines for correction. For each line, when the substrate passed by the hole, the velocity varied depending on the thickness to be corrected at different positions. In order to realize the two-dimensional figure correction, the substrate should be moved up and down by a specific distance. In this case, the distance was 8.5 mm.
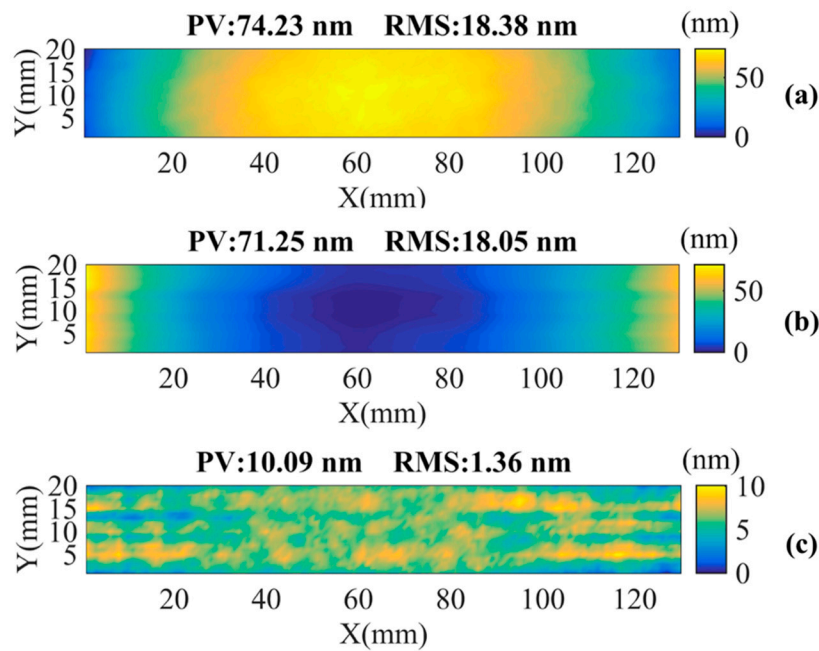
Figure 11. Simulated correction results. (**a**) Shape before correction. (**b**) Added thickness profile for the three-line correction. (**c**) Shape after the three-line correction.
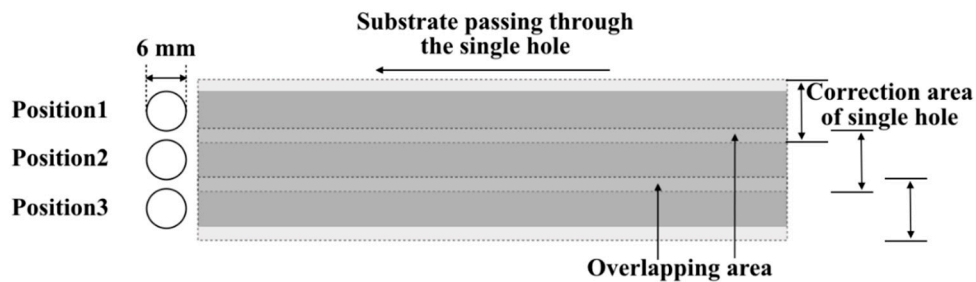
Figure 12. Schematic diagram of the correction process.

Figure 11b shows the added thickness profile of the three-line correction, and Figure 11c shows the simulated shape after the correction, where surface PV reduced from 74.23 nm to 9.62 nm, and the RMS reduced from 18.38 nm to 1.37 nm. In addition, there is a small gap in the overlapping area of the two neighboring correction lines in the simulation results, caused by the imperfect stitching of the correction contour from neighboring lines, and this problem has also been discovered in other correction methods, such as IBF [38]. This gap can be further improved by more iterative corrections or beam profile stitching optimization. In this simulation, only three-line stitching was performed to correct the shape, and a larger size correction can be carried out with more stitching corrections.

5. Conclusions

The particle distribution contour on substrates is important for shape correction by coating methods, especially for two-dimensional shape correction. Based on the existing theories for particle sputtering, angular distribution, and particle transport, a mask was added between the target and substrate to establish a complete model for generating a desired "beam profile". This model was well verified by the deposition experiments using different masks. Through the model, the effects of the mask on the particle distribution on the substrate were systematically investigated. Under the conditions of our experiments, as the distance from the mask to the substrate changed from 2 mm to 12 mm, the beam width changed from 2.79 mm to 14.84 mm for the 3 mm-diameter hole, and the beam width changed from 5.43 mm to 16.26 mm for the 6 mm-diameter hole. Moreover, as the mask gradually moved away from the substrate, the beam profile changed from convex to concave. The transition

from convex to concave happened when the distance from the mask to the substrate was around 6 mm for the 3 mm hole and 10 mm for the 6 mm hole. As near Gaussian beam profile is favorable in the figure correction process, these concave contours should be avoided. When the hole diameter is 3 mm, the maximum and minimum widths of near Gaussian beam profile are 2.79 mm and 4.97 mm, respectively. When the hole diameter is 6 mm, the maximum and minimum widths of near Gaussian beam profile are 5.43 mm and 10.54 mm, respectively. Generally, a larger hole size can give a larger beam profile and deposition rate. The distance from the mask to the substrate can affect both the beam shape and the beam size. The desired beam profile can be obtained by proper optimization of the hole size and the position of mask between the target and substrate. A two-dimensional shape correction of a plane mirror was demonstrated based on this model, and the surface PV reduced from 74.23 nm to 9.62 nm, and the RMS reduced from 18.38 nm to 1.37 nm by performing three-line corrections, and a larger area correction can be carried out with more stitching corrections. The newly established model will significantly improve the understanding of the mask-based deposition process, guide the optimization of a desired particle distribution contour, and enhance the capability of profile coating and differential deposition methods for manufacturing high-precision mirrors.

References

1. Mori, Y.; Yamauchi, Y.; Yamamura, K.; Mimura, H.; Saito, A.; Kishimoto, H.; Sekito, Y.; Kanaoka, M.; Souvorov, A.; Yabashi, M.; et al. Development of plasma chemical vaporization machining and elastic emission machining systems for coherent x-ray optics. In Proceedings of the X-Ray Mirrors, Crystals, and Multilayers, San Diego, CA, USA, 30–31 July 2001; pp. 30–42.

2. Yamauchi, K.; Mimura, H.; Inagaki, K.; Mori, Y. Figuring with subnanometer-level accuracy by numerically controlled elastic emission machining. *Rev. Sci. Instrum.* **2002**, *73*, 4028–4033. [CrossRef]

3. Kubota, A.; Shinbayashi, Y.; Mimura, H.; Sano, Y.; Inagaki, K.; Mori, Y.; Yamauchi, K. Investigation of the surface removal process of silicon carbide in elastic emission machining. *J. Electron. Mater.* **2007**, *36*, 92–97. [CrossRef]

4. Yuan, Z.; Dai, Y.F.; Xie, X.H.; Zhou, L. Ion Beam Figuring System for Ultra-Precise Optics. *Key Eng. Mater.* **2012**, *516*, 19–24. [CrossRef]

5. Peverini, L.; Kozhevnikov, I.V.; Rommeveaux, A.; Vaerenbergh, P.V.; Claustre, L.; Guillet, S.; Massonnat, J.Y.; Ziegler, E.; Susini, J. Ion beam profiling of aspherical X-ray mirrors. *Nucl. Instrum. Methods Phys. Res. A* **2010**, *616*, 115–118. [CrossRef]

6. Idir, M.; Lei, H.; Bouet, N.; Kaznatcheev, K.; Vescovi, M.; Lauer, K.; Conley, R.; Rennie, K.; Kahn, J.; Nethery, R.; et al. A one-dimensional ion beam figuring system for X-ray mirror fabrication. *Rev. Sci. Instrum.* **2015**, *86*, 105120. [CrossRef]

7. Mimura, H.; Yumoto, H.; Matsuyama, S.; Yamamura, K.; Sano, Y.; Ueno, K.; Endo, K.; Mori, Y.; Yabashi, M.; Tamasaku, K.; et al. Relative angle determinable stitching interferometry for hard x-ray reflective optics. *Rev. Sci. Instrum.* **2005**, *76*, 045102. [CrossRef]

8. Thiess, H.; Lasser, H.; Siewert, F. Fabrication of X-ray mirrors for synchrotron applications. *Nucl. Instrum. Methods Phys. Res. A* **2010**, *616*, 157–161. [CrossRef]

9. Handa, S.; Mimura, H.; Yumoto, H.; Kimura, T.; Matsuyama, S.; Sano, Y.; Yamauchi, K. Highly accurate differential deposition for X-ray reflective optics. *Surf. Interface Anal.* **2008**, *40*, 1019–1022. [CrossRef]

10. Alcock, S.G.; Cockerton, S. A preferential coating technique for fabricating large, high quality optics. *Nucl. Instrum. Methods Phys. Res. A* **2010**, *616*, 110–114. [CrossRef]

11. Kilaru, K.; Ramsey, B.D.; Gubarev, M.V. Development of differential deposition technique for figure corrections in grazing incidence X-ray optics. In Proceedings of the Optics for EUV, X-Ray, and Gamma-Ray Astronomy IV, San Diego, CA, USA, 4 August 2009; p. 743719.

12. Kilaru, K.; Ramsey, B.D.; Kolodziejczak, J.; Atkins, C. Improving x-ray optics via differential deposition. In Proceedings of the Optics for EUV, X-Ray and Gamma-Ray Astronomy VIII, San Diego, CA, USA, 8–10 August 2017; p. 103991F.

13. Ice, G.E.; Chung, J.-S.; Tischler, J.Z.; Lunt, A.; Assoufid, L. Elliptical x-ray microprobe mirrors by differential deposition. *Rev. Sci. Instrum.* **2000**, *71*, 2635–2639. [CrossRef]

14. Liu, C.; Conley, R.; Assoufid, L.; Cai, Z.; Qian, J.; Macrander, A.T. From Flat Substrate to Elliptical KB Mirror by Profile Coating. In Proceedings of the 8th International Conference on Synchrotron Radiation Instrumentation, San Francisco, CA, USA, 25–29 August 2003; pp. 704–707.

15. Bing, S.; Chian, L.; Jun, Q.; Wenjun, L.; Assoufid, L.; Khounsary, A.; Conley, R.; Macrander, A.T. Platinum Kirkpatrik-Baez mirrors for a hard x-ray microfocusing system made by profile coating. In Proceedings of the Advances in X-Ray/EUV Optics and Components V, San Diego, CA, USA, 2–3 August 2010; p. 78020G.

16. Liu, C.; Assoufid, L.; Conley, R.; Macrander, A.T.; Ice, G.E.; Tischler, J.Z. Profile coating and its application for Kirkpatrick-Baez mirrors. *Opt. Eng.* **2003**, *42*, 3622–3628. [CrossRef]

17. Liu, C.; Conley, R.; Macrander, A.T. Functional profile coatings and film stress. *J. Vac. Sci. Technol.* **2004**, *22*, 1610–1614. [CrossRef]

18. Zhang, Z.; Qi, R.Z.; Yao, Y.Y.; Shi, Y.N.; Li, W.B.; Huang, Q.S.; Yi, S.Z.; Zhang, Z.; Wang, Z.S.; Xie, C. Improving Thickness Uniformity of Mo/Si Multilayers on Curved Spherical Substrates by a Masking Technique. *Coatings* **2019**, *9*, 851. [CrossRef]

19. Yingna, S.; Runze, Q.; Yufei, F.; Qiushi, H.; Zhengxiang, S.; Zhanshan, W. Microstructure, roughness, and stress properties of silicon coatings for shape correction of Kirkpatrick-Baez mirrors. *Opt. Eng.* **2019**, *58*, 015103. [CrossRef]

20. Lizhen, Z.; Enze, W.; Zhengquan, Z.; Lige, W.; Yongsheng, Z.; Shaowu, C.; Xiaoan, Y. Study on new technology of removing abandoned tobacco zinc plate coating by using mechanical method. *Adv. Mater. Res.* **2012**, *472–475*, 2944–2947. [CrossRef]

21. Mizuno, K.; Habuka, H.; Ishida, Y.; Ohno, T. In Situ Cleaning Process of Silicon Carbide Epitaxial Reactor for Removing Film-Type Deposition Formed on Susceptor. *Mater. Sci. Forum* **2016**, *858*, 237–240. [CrossRef]

22. Pa, P.S. A removing process for multilayer nano thin-film structures on the hard disk surface. *Int. J. Adv. Manuf. Technol.* **2014**, *70*, 459–467. [CrossRef]

23. Zubar, T.I.; Fedosyuk, V.M.; Trukhanov, A.V.; Kovaleva, N.N.; Astapovich, K.A.; Vinnik, D.A.; Trukhanova, E.L.; Kozlovskiy, A.L.; Zdorovets, M.V.; Solobai, A.A.; et al. Control of growth mechanism of electrodeposited nanocrystalline NiFe films. *J. Electrochem. Soc.* **2019**, *166*, D173–D180. [CrossRef]

24. Warcholinski, B.; Gilewicz, A.; Lupicka, O.; Kuprin, A.S.; Tolmachova, G.N.; Ovcharenko, V.D.; Kolodiy, I.V.; Sawczak, M.; Kochmanska, A.E.; Kochmanski, P.; et al. Structure of CrON coatings formed in vacuum arc plasma fluxes. *Surf. Coat. Technol.* **2017**, *309*, 920–930. [CrossRef]

25. Zavaleyev, V.; Walkowicz, J.; Kuznetsova, T.; Zubar, T. The dependence of the structure and mechanical properties of thin ta-C coatings deposited using electromagnetic venetian blind plasma filter on their thickness. *Thin Solid Films* **2017**, *638*, 153–158. [CrossRef]

26. Broadway, D.M.; Platonov, Y.Y.; Gomez, L.A. Achieving desired thickness gradients on flat and curved substrates. In Proceedings of the 1999 X-Ray Optics, Instruments, and Missions II, Denver, CO, USA, 18–20 July 1999; pp. 262–274.

27. Mahieu, S.; Buyle, G.; Depla, D.; Heirwegh, S.; Ghekiere, P.; De Gryse, R. Monte Carlo simulation of the transport of atoms in DC magnetron sputtering. *Nucl. Instrum. Methods Phys. Res. B* **2006**, *243*, 313–319. [CrossRef]

28. Yamazaki, T.; Matsuda, K.; Nakatani, H. Effect of angular distribution of ejected atoms from a target on the uniformity of thickness and composition of MoSix sputtering films. *Jpn. J. Appl. Phys.* **1990**, *29*, 1304–1309. [CrossRef]

29. Ekpe, S.D.; Bezuidenhout, L.W.; Dew, S.K. Deposition rate model of magnetron sputtered particles. *Thin Solid Films* **2005**, *474*, 330–336. [CrossRef]

30. Zhang, J.; Wang, Z.; Tao, Z.; Pan, J. The angular distributions of sputtered indium atoms at different temperature. *J. Mater. Sci. Lett.* **1993**, *12*, 747–748. [CrossRef]

31. Andersen, H.H.; Stenum, B.; Sorensen, T.; Whitlow, H.J. Angular distribution of particles sputtered from Cu, Pt, and Ge targets by keV Ar+ ion bombardment. *Nucl. Instrum. Methods Phys. Res. B* **1985**, *B6*, 459–465. [CrossRef]

32. Chang-Gyu, K.; Won-Jong, L. An angular distribution function for the sputter-depositing atoms and general equations describing the initial thickness profile of a thin film deposited inside a via and trench by sputtering. *Thin Solid Films* **2010**, *519*, 74–80. [CrossRef]

33. Escrivao, M.L.; Pereira, P.J.S.; Ferreira, J.L.; Teixeira, M.R.; Maneira, M.J.P. Argon temperature and density versus the input power in a high pressure planar magnetron discharge. *Vacuum* **2002**, *64*, 367–371. [CrossRef]

34. Westwood, W.D. Calculation of deposition rates in diode sputtering systems. *J. Vac. Sci. Technol.* **1978**, *15*, 1–9. [CrossRef]

35. Chang, S.A.; Skolnik, M.B.; Altman, C. High rate sputtering deposition of nickel using Dc magnetron mode. *J. Vac. Sci. Technol. A* **1986**, *4*, 413–416. [CrossRef]

36. Ozimek, M.; Wilczynski, W.; Szubzda, B. Magnetic thin film deposition with pulsed magnetron sputtering: Deposition rate and film thickness distribution. In Proceedings of the 8th National Scientific Conference Advances in Electrotechnology, Jamrozowa Polana, Poland, 23–25 September 2015; p. 012009.

37. Ma, S.; Shen, Z.; Chen, S.; Wang, Z. Fractal surface for calibration of an optical profiler. *Optik* **2014**, *125*, 4685–4688. [CrossRef]

38. Zhang, X.; Zeng, X.; Hu, H.; Luo, X. Manufacturing and testing large SiC mirrors in an efficient way. In Proceedings of the Optical Systems Design 2015: Optical Fabrication, Testing and Metrology V, Jena, Germany, 7 September 2015; p. 96280S.